Metrics of High Cofluctuation and Entropy to Describe Control of Cardiac Function in the Stellate Ganglion

Nil Z. Gurel[1*,†], Koustubh B. Sudarshan[3,†], Joseph Hadaya[1,2], Alex Karavos[3], Taro Temma[1], Yuichi Hori[1], J. Andrew Armour[1], Guy Kember[3], Olujimi A. Ajijola[1,2]

***For correspondence:** nil@ucla.edu (FMS)

[†]These authors contributed equally to this work

[1] UCLA Cardiac Arrhythmia Center and UCLA Neurocardiology Research Program of Excellence, Los Angeles, CA; [2]UCLA Molecular, Cellular, and Integrative Physiology Program, Los Angeles, CA; [3]Department of Engineering Mathematics and Internetworking, Dalhousie University, Nova Scotia, Canada

Abstract Cardiac neural control requires dynamic adaptation of mechanical and electrical indices to meet blood flow demands. The control system receives inputs to coordinate cardiac function, producing "functional" outputs such as blood pressure and heart rate. Bilateral stellate ganglia (SG) integrate inputs and produce efferent cardiopulmonary sympathetic outputs. We investigate network processing of cardiopulmonary transduction by SG neuronal populations in porcine with chronic pacing-induced heart failure and control subjects during extended in-vivo extracellular microelectrode recordings. We derive network-level spatiotemporal dynamic signatures based on linking neuronal population cofluctuation and examine differences in "neural specificity" of SG network activity to cardiac cycle phases. Information processing and cardiac control in chronic heart failure by the SG, relative to controls, exhibits: i) more frequent, short-lived, high magnitude cofluctuations, ii) greater variation in neural specificity to cardiac cycles, and iii) neural network activity and cardiac control linkage that depends on disease state and cofluctuation magnitude.

Introduction

Neural control of cardiac function involves adaptive adjustment of mechanical and electrical activity to meet the organism's demand for blood flow. This cardioneural control scheme consists of neural populations in the central, peripheral, and intrinsic cardiac nervous systems. Interactions among components of the cardiac nervous system highlight that these neural populations work in concert, rather than as independent, singular processing units (***Ardell et al., 2016***). From an information processing standpoint, the operation of these interconnected neural networks has evolved to coordinate cardiac function on a beat-by-beat basis, producing the "functional" outputs of this control scheme such as blood pressure, heart rate, or respiratory pressure and rate. Localized adaptations in the cardioneural network in response to pathology can cause an evolution of global network properties with heightened risk of poor outcomes without measurable evidence from these functional outputs (***Deyell et al., 2015***; ***Kember et al., 2013***).

There is a current focus on understanding cardioneural network processing within the stellate ganglion (SG), a collection of nerves serving as the major source of sympathetic input to the

heart(***Mehra et al., 2022***). The SG (located in either side of the neck) operates as an integrative layer within the control hierarchy where it processes central cardiac inputs to the heart, receives cardiac feedback, and projects efferent control outputs to the heart. In pathological states such as heart failure (HF), morphological and neurochemical remodeling of SG neurons has been reported in both animal models (***Ajijola et al., 2013***; ***Han et al., 2012***; ***Ajijola et al., 2015***; ***Nakamura et al., 2016***) and in humans (***Ajijola et al., 2020***, ***2012b***). Due to its key role in proarrhythmic neural signaling and convenience in surgical accessibility, clinical interventions targeting SG are used to treat various cardiovascular conditions (***Vaseghi et al., 2012***, ***2017***; ***Ajijola et al., 2012a***). It has also been established that an enhanced cardiac sympathetic afferent reflex contributes to sympathoexcitation and pathogenesis of heart failure (***Wang and Zucker, 1996***; ***Ma et al., 1997***; ***Chen et al., 2015***; ***Wang et al., 2017***, ***2008***, ***2014***; ***Gao et al., 2005***, ***2007***). Despite these novel interventions and general understanding, SG clinical therapy will remain largely unexplored without greatly improved understanding of SG neuronal information processing in healthy versus pathological states. Prior studies examining the SG neural activity have been limited to in vivo extracellular recordings (***Armour, 1983***, ***1986***; ***Armour et al., 1998***; ***Yoshie et al., 2020***, ***2018***).

Recently, we explored network processing of cardiopulmonary transduction by SG neuronal populations in healthy porcine, defining a novel metric 'neural specificity' that measures specificity of neural firing patterns to cardiopulmonary signals (***Sudarshan et al., 2021***). This metric is contrastive and a measure of the difference between the probability density function (PDF) of neural 'sampling' of a control target relative to the same in the random sampling limit. While the target, left ventricular pressure (LVP) considered here is periodic this is not a necessary condition for use of the specificity metric; it is also applicable to aperiodic signals in an event-based fashion.

In the current work, we investigate differences in information transfer between control and heart failure porcine models with multi-channel electrode arrays. We first uncover network-level spatiotemporal dynamic signatures by quantifying short-lived high cofluctuation events in neural activity. Second, we study coherence and consistency in the evolution of neural specificity with respect to the control target. Third, we expose differences in neural specificity and its coherence and consistency, via entropy, inside and outside cofluctuation events. These differences are considered for control and heart failure models and quantify differences in the maintenance of function between these groups.

Methods

Animal Experiments

Fig. 1 presents the conceptual overview and study design. The study was performed under a protocol approved by the University of California Los Angeles (UCLA) Animal Research Committee (ARC), in compliance with the UCLA Institutional Animal Care and Use Committee (IACUC) guidelines and the National Institutes of Health (NIH) Guide for the Care and Use of Laboratory Animals. Fig. 1D-E summarizes the studied animal groups and experimental pipeline. Male Yorkshire pigs $(n = 17)$ weighing $57.5 \pm 12kg$ $(mean \pm SD)$ were studied as control $(n = 6)$ and HF model $(n = 11)$ groups. For SG neural data collection, the animals were sedated with tiletamine and zolazepam (Telazol, 4-8mg/kg) intramuscularly, intubated, and maintained under general anesthesia with inhaled isoflurane (2%). Continuous intravenous saline $(8 - 10ml/kg/h)$ was infused throughout the protocol and animals were temperature maintained using heated water blankets $(37^oC - 38^oC)$.

Median sternotomy by an incision down the midline of the entire sternum was performed to have a wide view of the thoracic region (Fig. 1A). The pericardium was opened to expose the heart and both stellate ganglia. After surgical procedures, animals were transitioned to alpha-chloralose anesthesia ($6.25mg/125mL$; $1mL/kg$ for bolus, $20 - 35mL/kg$ or titrated to effect for maintenance) with supplemental oxygen $(2L/minute)$ for in vivo neural recordings from the left stellate ganglion. The left carotid artery was exposed, and a pressure catheter (SPR350, Millar Inc., Houston, TX) was inserted to continuously monitor left ventricular pressure (LVP). Additionally, three-lead surface

electrocardiogram (ECG) and respiratory pressure (RP) were monitored continuously, and sampled at $1kHz$. Arterial blood gas contents were monitored at least hourly to ensure appropriate experimental conditions. At the end of the protocol, animals were euthanized under deep sedation of isoflurane and cardiac fibrillation was induced.

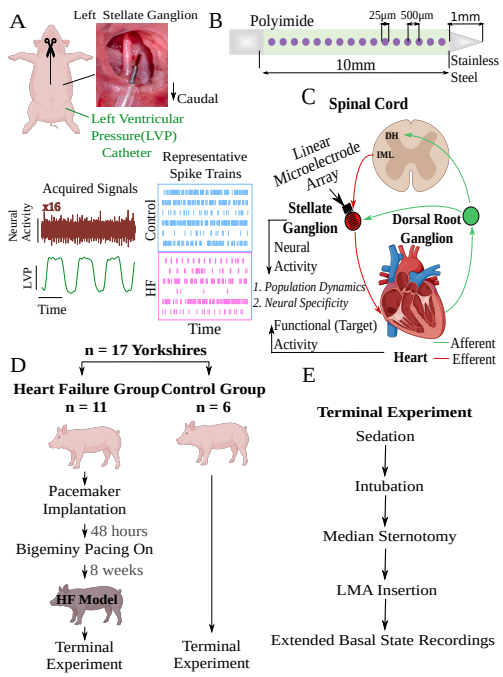

Figure 1. Experimental workflow and overall concept. A) A linear microelectrode array (LMA) was inserted to the left stellate ganglion (SG) for each animal. A total of 16 channels of neural activity were collected along with simultaneous left ventricular pressure (LVP). Representative spike trains are displayed for each animal group. B) Specifications of the LMA. C) Conceptual representation of this work. SG receives efferent and afferent information from the spinal cord's intermediolateral complex (IML) and dorsal root ganglion, respectively, and transmits efferent information to the heart. In this work, we investigate neural activity and its relationship to cardiac function as represented by a control target such as LVP. D) Among 17 Yorkshire pigs, 11 had heart failure induced by ventricular pacing, and 6 were in control group. SG recordings were collected at terminal experiments for both groups. E) Experimental flow descripting the surgical preparation for the recordings. DH: Dorsal horn.

The heart failure model was created with implanted pacemakers (Viva Cardiac Resynchronization Therapy–Pacemaker, Biotronik, Lake Oswego, OR), as previously described (***Hori et al., 2021***), and summarized in Fig. 1D. After implantation, animals had a recovery period of 48 hours and chronic bigeminy pacing was initiated from the right ventricle. This process produces premature ventricular contractions (PVCs) which lead to cardiomyopathy, also known as PVC-induced cardiomyopathy (***Blaye-Felice et al., 2016***). To confirm the progression of cardiomyopathy, echocardiography was performed, before and after implantation. After the animals have been confirmed to have cardiomyopathy (referred as HF animals) at eight weeks after implantation, surgical procedures described in Fig. 1E were performed, and extracellular recordings were obtained from the left stellate ganglion, shown in Fig. 1A. It should be noted that a subset of HF animals $(n = 6)$ underwent an intervention, epicardial application of resiniferatoxin (RTX) to study its effects on the progression of cardiomyopathy as a separate study. However no significant effect of RTX was noted in any of the echocardiographic, serum, physiological, and autonomic tests (***Hori et al., 2021***). Hence, in this work, we combined RTX-treated HF animals with untreated HF animals.

SG Neural Recordings and Experimental Protocol

For each animal, a 16-channel, linear, single shank microelectrode array (LMA, Microprobes, Gaithersburg, MD) was inserted in the craniomedial pole of the left stellate ganglion (Fig. 1A). The LMA consisted of a polyimide tube of $0mm$ that contains recording sites, and a stainless steel tip of $1mm$ (Fig. 1B). Polyimide tube hosted a total of 16 platinum-iridium recording sites with $25\mu m$ radius, separated by $500\mu m$ intra-electrode spacing. A microelectrode amplifier (Model 3600, A-M Systems, Carlsborg, WA) was used to amplify (gain of $1000 - 2500$) and filter ($300Hz - 3kHz$ band-pass filter) the acquired signals. The signals were transferred to a data acquisition platform (Power 1401, Cambridge Electronic Design, Cambridge, UK) and recorded using Spike2 software (Cambridge Electronic Design, Cambridge, UK). All data were processed in Python and MATLAB.

We have shown in our previous work that increases in spike rate occur within 90-minutes of

electrode insertion, hence a stabilization time is required after the insertion takes place (***Sudarshan et al., 2021***). To accomplish this, all experiments included extended basal state recordings lasting approximately three hours.

Signal Processing and Time Series Analysis

Signal Processing Pipeline

A high-level description of the signal processing pipeline is in Fig. 2. Supporting codes are made available at GitHub (https github.comKoustubh2111Cofluctuation-and-Entropy-Code-Data). In summary, Pearson's cross correlation is used to construct the coactivity matrix as the collection of cross correlations between all possible channel pairs. The coactivity matrix is computed at each timestamp and associated with a window of past neural activity (Fig. 2, 'Coactivity' block). This computation yields a causal sliding window of coactivity matrices referred to as the 'coactivity time series'.

Discrete events of high cofluctuation occurring in the coactivity time series are defined using two thresholds: (i) the coactivity time series is mapped to a univariate 'cofluctuation time series' where, at each timestamp, the percentage of coactivity matrix members exceeding a threshold C is found, and (ii) discrete 'events' are defined as those timestamps when up-crossings of the cofluctuation time series through a second threshold T occur. The method used to choose the (C, T) pair, detailed in this section, generates discrete event timestamps and allows for the computation of the event rate (ER) mean and standard deviation (STD) statistics, which are used later in the statistical analyses. These cofluctuation events are regions that expose shifts in neural processing within the SG. These events are linked to function through the consideration of how neural specificity differs inside and outside cofluctuation events in control and heart failure animals.

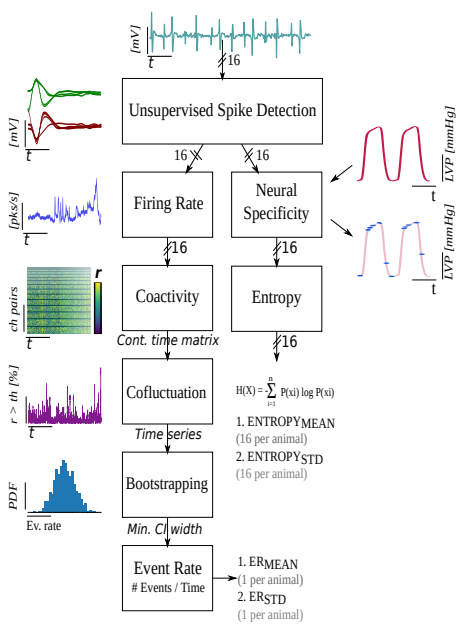

Figure 2. Signal Processing Block Diagram.

The relationship between a control target such as LVP and neural activity at each channel is quantified via a continuously varying neural specificity (***Sudarshan et al., 2021***) (Fig. 2, 'Neural Specificity' block). The neural specificity is contrastive since it is the difference between the PDF of neural sampling of a target and the same found from random sampling. The neural activity in the SG is known to be a mixture of afferent, efferent, and local circuit activity derived from local circuit neurons with inputs from multiple sources. It in this sense that we define neural computation; when we observe the specificity to the target operating above or below the random sampling limit. Neural specificity is a multivariate signal measured across multiple target states at each channel as a function of time. This is reduced, for each channel, to a univariate time series by constructing its coherence in terms of entropy. The evolution of coherence in time provides access to the dynamics or consistency of neural computation. Detailed information about each signal processing step is provided in this section.

Unsupervised Spike Detection

We use a competitive, adaptive threshold, unsupervised approach for neural spike detection (***Sudarshan et al., 2021***). The algorithm initializes plus and minus barriers at the plus or minus signal

maximum amplitude. The barriers are respectively lowered or raised until the plus or minus barrier 'wins the competition' and is the first to yield a minimal number of crossings. Detected spike regions are masked as a zero signal and the process repeated with barrier sizes further reduced in subsequent iterations. The competition is halted when one barrier is first to reach a minimal barrier height.

Cofluctuation and Event Rate Definitions

Coactivity Matrix

A $16x16$ correlation matrix, $4x4$ version is shown in Fig. 3B for $n = 4$ channels, is used to investigate spatial coherence among neural populations in different regions of the SG spanned by 16 electrodes (Supplementary Fig. 1 shows such a correlation matrix). The coactivity matrix at each timestamp is found from Pearson's cross-correlation between all possible pairs of causal channel sliding mean and standard deviation of spike rate. The sliding mean and standard deviation of spike rate are respectively referred to as $Spike_{RateMEAN}$ and $Spike_{RateSTD}$, and are on the y-axis of Fig. 3A. These are referred to as 'spike rate' in what follows when both are implied. To fix ideas, consider Pearson's cross correlation coefficient (R) between channels 1 and 2, labeled as R_{12}: namely, the red and blue windows respectively in Fig. 3A. In the coactivity matrix depicted in Fig. 3B, there are $n = 4$ channels, hence $n - 1 = 3$ super-diagonals. These are vertically stacked in Fig. 3C at each timestamp beginning with the first super-diagonal as R_{12}, R_{23}, R_{34}. In this way, adjacent channels are placed at the bottom followed by super-diagonals corresponding to 2 and 3 channels of separation. The super-diagonal of the 16-channel LMA electrode correlation matrix has $n = 16$ channels separated by $500\mu m$ and $n(n-1)/2 = 120$ possible pairwise correlations (See Supplementary Fig. 1 for an example). This yields 120 rows in the stacked version of the coactivity matrix at each timestamp analogous to the same visualized in Fig. 3C for $n = 4$ channels.

Cofluctuations and Event Rate

The univariate cofluctuation time series is the percentage of coactivity matrix members, at each timestamp, that exceed a threshold Pearson's $R > C$, depicted in Fig. 3D. Discrete events are considered to begin at a time of up-crossing of the univariate cofluctuation time series through a threshold T. Each event ends at a down-crossing some time later, as shown in Fig. 3E. These discrete events capture spatiotemporal zones of high SG coactivity. Up-crossing times are respectively converted to an event rate (ER_{MEAN}, ER_{STD}) for the $(Spike_{RateMEAN}, Spike_{RateSTD})$ over a duration

$$(ER_{MEAN}, ER_{STD}) = \frac{(N_{MEAN}, N_{STD})}{EventsDuration} \tag{1}$$

where event rate, ER, has units $1/s$ and (N_{MEAN}, N_{STD}) are the number of upcrossings within the $EventsDuration$ considered.

Cofluctuation Probability Distribution

The cofluctuation time series at each threshold C (as in Fig. 3D) qualitatively approximates a log-normal distribution. The log-normal fits of cofluctuation time series (Fig. 7) are obtained using Python SciPy package, with statistics and random numbers module (scipy.stats) (***Virtanen et al., 2020***).

Bootstrapping and Selection of Convergent Thresholds

The event rate is calculated based on a pair of thresholds (C, T). The first threshold (C, Fig. 3D) is used to reduce the coactivity time series of matrices to a univariate cofluctuation time series. The univariate series is the percentage of coactivity matrix entries exceeding C at each timestamp. The cofluctuation time series is then used to define regions of high cofluctuation based on intervals where the time series exceeds a second threshold T. These regions are discrete 'events' that begin and end when the cofluctuation time series respectively up- and down-crosses through T (Fig. 3D). Bootstrapping of the event up-crossing timestamps is used to construct the event rate histogram of a threshold pair (C, T).

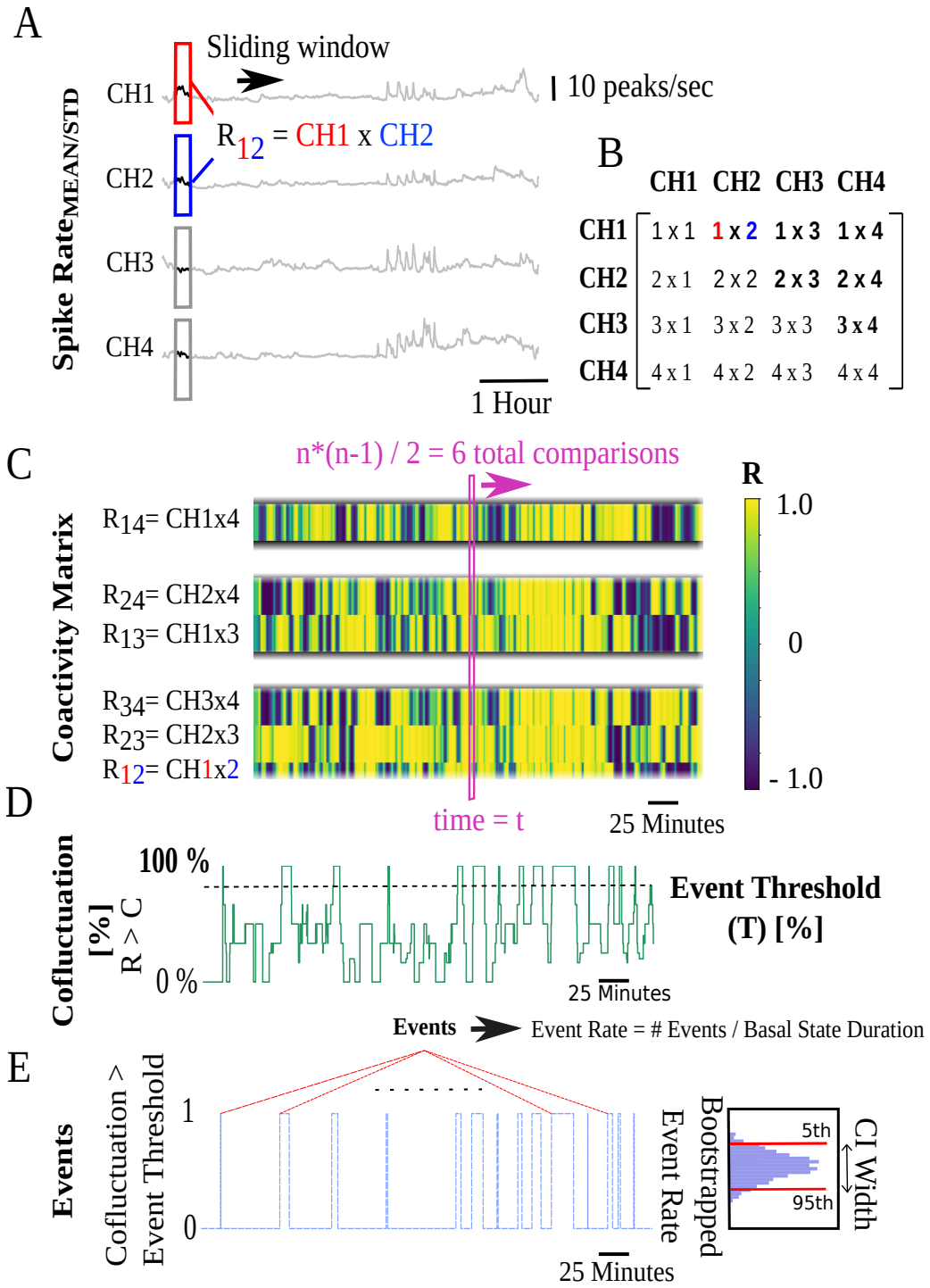

Figure 3. Coactivity matrix and event rate (ER) computation pipeline illustrated for 4-channels. A) Pearson's cross correlation coefficients (R) of pairwise sliding spike rate windows for 4 channels. B) R values for cross correlation of 'i' and 'j' channels are stored in the 'i' and 'j' positions of a $4x4$ matrix at each timestamp. C) Coactivity matrix super-diagonals at each timestamp are vertically stacked. At each timestamp t, $n(n-1)/2 = 6$ unique cross-correlations are possible corresponding to super-diagonals with 3, 2, and 1 members. The y-axis begins at the bottom with the 3 members of the first super-diagonal followed by subsequent super-diagonals. Colors represent the R value. D) Cofluctuation time series are the percentage of Pearson's R values at each timestamp that exceed a cofluctuation threshold (C). E) Discrete events correspond to time intervals when cofluctuations show an up/down crossing through an event threshold (T).

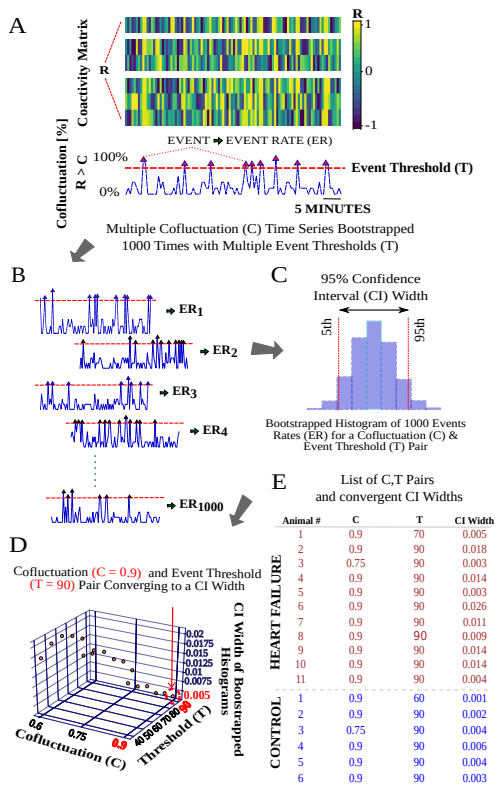

Animal #	C	T	CI Width
1	0.9	70	0.005
2	0.9	90	0.018
3	0.75	90	0.003
4	0.9	90	0.014
5	0.9	90	0.003
6	0.9	90	0.026
7	0.9	90	0.011
8	0.9	90	0.009
9	0.9	90	0.014
10	0.9	90	0.014
11	0.9	90	0.004
1	0.9	60	0.001
2	0.9	90	0.002
3	0.75	90	0.004
4	0.9	90	0.006
5	0.9	90	0.004
6	0.9	90	0.003

Figure 4. Cofluctuation bootstrapping pipeline for individualized event rate (ER) for each animal. A) Coactivity matrix and cofluctuation time series for a cofluctuation threshold and event threshold pair (C, T). B) Cofluctuation time series with depicted events (red triangles are upcrossing timestamps) for a range of (C, T) pairs. C) Bootstrapped histogram of ERs for a single (C, T) pair with 95% confidence interval (CI) width. D) Threshold pair (C, T) is chosen for an animal given non-zero ER and ER convergence. Depicted CI widths are found at all of the depicted 18 (C, T) pairs available on the axes grid. E) List of (C, T) pairs that show ER convergence with CI widths for each animal. Fig. 4A is further explained in Supplementary Figure labelled Fig. 11.

These histograms lead to a convergent choice of threshold pairs (C, T). The convergent (C, T) pair is taken as the location in (C, T) space where the confidence interval (CI) width shows apparent convergence. An upper bound on (C, T) is imposed so that there is sufficient data to compute the desired statistics.

The procedure is visualized in Fig. 4A using a surrogate coactivity matrix R. Univariate cofluctuation time series are created from a range of thresholds C that inclusively vary over 60-90% with 15% increments. Discrete events are determined, shown as red up-crossing triangles in Fig. 4 A-B, for each of the thresholds C and considered over an inclusive range 40-90% with 10% increments of event thresholds T. Bootstrapped events provided the associated ER histogram of each (C, T) threshold pair and desired 95% CI width of each animal (Fig. 4C). A convergent (C, T) pair for an animal is provided in Fig. 4D $(C, T = 0.9, 90)$, that converged to a 95% CI width of 0.005. Following this approach, convergent (C, T) pairs and bootstrapped CI widths are listed for each animal in Fig. 4E.

Using these individualized convergent (C, T) pairs, original (i.e., not bootstrapped) data are used to calculate event rates for each animal. Note that event rates are calculated from both spike rate mean and standard deviation coactivity matrices, and referred to as ER_{MEAN} and ER_{STD}. These are then used in statistical analyses (one ER_{MEAN} and one ER_{STD} per animal) as shown in Fig. 2. A similar procedure was performed in the literature using neuroimaging time series data based on Pearson's R (***Esfahlani et al., 2020***) however the threshold selection process was qualitative. In this work, we have developed a quantitative approach for threshold selection.

Neural Specificity

The neural specificity metric (***Sudarshan et al., 2021***), Fig. 5, is used to evaluate the degree to which neural activity is biased toward control target states taken here as LVP. Briefly, this metric is computed in three stages

1. *Neural Sampling* The value of the target state (LVP) is 'sampled' at the timestamp of each spike occurrence. This sampling is assumed to approximate a quasi-stationary distribution over a causal (backward in time) sliding window of spiking activity that is updated at each new timestamp. The distribution is approximated as a normalized and sliding histogram of neurally sampled target states (LVP).

2. *Random Sampling* The normalized, sliding random sampling histogram is found at each spike occurrence in (1), but based on *all* available LVP samples within the same causal window referenced in (1), which approximates the random sampling limit.
3. *Neural Specificity* The normalized, sliding random sampling histogram (2) is subtracted from its neural sampling counterpart (1) to form the neural specificity contrastive measure.

Subtraction of the random sampling histogram from the neural sampling histogram allows for the discovery of the degree to which neural activity is biased, or specific, toward sampling control target states (LVP here) relative to random sampling. To explain the construction of the metric with LVP, a representative window is shown in Fig. 5A with the spikes shown as green dots over LVP waveform. The following steps outline the construction of the neural specificity metric, A, for a representative LVP window

1. *Neural Sampling*
   Following (***Sudarshan et al., 2021***), the normalized sliding window histogram of neurally sampled LVP_j at all spike times t_j and taken over M bins is defined for bin k as

$$H(SLVP_j)_k = \frac{h(SLVP_j)_k}{\Sigma_{k=1}^{k=m} h(SLVP_j)_k} \tag{2}$$

   Eq. (2) approximates the distribution of neural sampling of the target LVP at the green dots over a causal window in Fig. 5A. The resulting normalized histogram shown for one timestamp (green line) in Fig. 5B.
2. *Random Sampling* The normalized sliding window histogram at the random sampling limit of LVP_j is computed as in (1), but based on *all* LVP samples within the same causal window and defined as $H(LVP_j)_k$. This is depicted as sampling of the pink line in Fig. 5A over the same causal window used to describe neural sampling of LVP. The result is shown for one timestamp as the normalized histogram (pink line) in Fig. 5B.
3. *Neural Specificity* The neural specificity, A_{jk}, for bin k is

$$A_{jk} = H(SLVP_j)_k - H(LVP_j)_k \tag{3}$$

   A_{jk} is mapped to three levels $(less,\ same,\ greater)$ relative to random sampling. These are respectively defined as $(-1, 0, 1)$ and depicted as $(purple,\ teal,\ yellow)$ in Fig. 5C-D. As such, given the mapping threshold $\alpha > 0$ it follows that $(A_{jk} < -\alpha, A_{jk} < \alpha, A_{jk} > \alpha])$ is respectively $(-1, 0, 1)$ implying $(less,\ same,\ greater)$ neural specificity relative to random sampling and visually represented as $(purple,\ teal,\ yellow)$.

Entropy Definitions

Entropy

The neural specificity is reduced from a multivariate signal to a univariate signal by computing the Shannon entropy at each timestamp of the mapped neural specificity metric (Fig. 2, Eq. (3) mapping description). The entropy of the absolute change between adjacent normalized histogram bins is a measure of coherence in neural specificity. The absolute change in the mapped A_{jk} at time t_j and between adjacent bins $(k,\ k+1),\ k = 1, ..., m-1$ is the set $\Delta A_j = (0, 1, 2)$ with members $\Delta A_{ji}, i = 1, 2, 3$. Using a base 3 logarithm to scale the entropy between 0 and 1, the entropy E_j of the difference in the mapped A_{jk} at each timestamp t_j.

$$E_j = -\Sigma_{\Delta A_{ji}=1}^{3} p(\Delta A_{ji}) \ln_3(p(\Delta Aji)) \tag{4}$$

This unequally-sampled series is interpolated to the equally-sampled time series E.

Event Entropy

The neural specificity provides a measure of specificity, or bias, of neural activity to target states. On the other hand, unusually high and short-lived cofluctuations indicate intervals in time, or 'events', when coactivity between the sliding mean and/or standard deviation of neural activity measured between channel pairs implies that SG processing has undergone sudden changes. Functional relevance of cofluctuation events is found here by considering the extent to which neural specificity to the target (LVP here) is similar or different inside and outside these events.

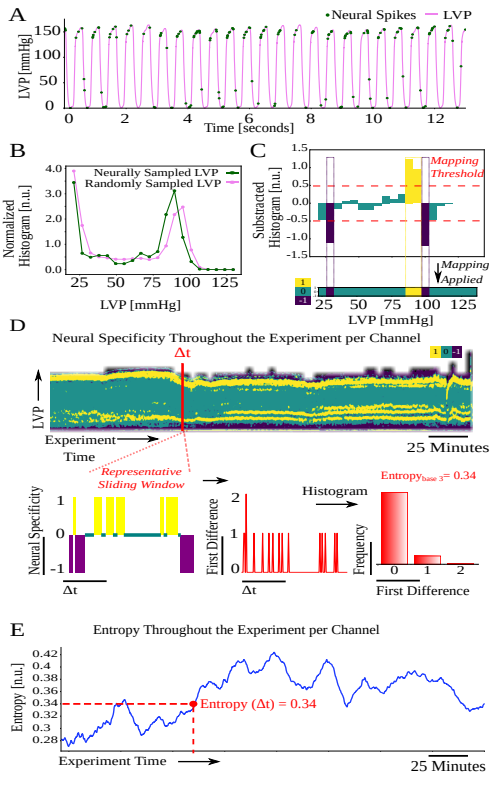

Figure 5. Neural specificity and entropy computation pipeline. A) Segment of neural specificity showing left ventricular pressure (LVP) and neural spikes. Spiking activity is observed to be more specific or biased (yellow), over random sampling, to LVP just below systolic pressures. B) Normalized histograms of random sampled LVP and neurally sampled LVP. C) Bars show subtracted histograms and colors indicate the specificity thresholded with $\alpha = 0.5$: specificity exceeding α is yellow, below $-\alpha$ is blue, and between the bounds $(-\alpha, \alpha)$ is teal. D) Sliding neural specificity time series (top) for a selected sliding window width Δt. Entropy of neural specificity, computed from red highlighted window of width Δt, absolute difference (shown for a sample at bottom). E) Entropy time series corresponding to the overall experiment, entropy sample computed from steps in D.

Therefore, the functional relevance of cofluctuations in SG neural activity is examined by breaking the time-evolution of entropy of neural specificity into regions: 'event' regions (within event intervals) and 'non-event' regions (outside event intervals). The mean and standard deviation of event and non-event entropy time series per channel are computed for each experiment and collectively referred to as 'event entropy' where this is convenient.

Dataset and Statistical Analysis

Statistical analyses are performed in MATLAB Statistics & Machine Learning Toolbox (version R2021a) and Python SciPy Library (version 3.8.5).

Sample Size Breakdown

Two channels were excluded from two animals due to insufficient signal quality. Within event rate analyses, all animals had sufficient neural data ($n = 17$ animals, 6 control, 11 HF). Entropy analyses for 3 HF animals were excluded due to insufficient LVP quality resulting in $n = 14$ animals (6 control, 8 HF).

Outcome Measures

Within the signal processing pipeline described in Fig. 3, the event rate measures, ER_{MEAN} and ER_{STD}, are used to summarize the cofluctuation time series for each animal. A mean and standard deviation of the 16 channel-wise entropy time series results in 32 measures of entropy per animal (16 for $Entropy_{MEAN}$ and 16 for $Entropy_{STD}$ per animal).

Statistical Analysis

For variables that result in a single number per animal (such as ER_{MEAN} and ER_{STD}, Fig. 6A-B), independent samples t-tests or Wilcoxon rank-sum tests are respectively used for normal or non-normal data (normality assessed by Shapiro-Wilk) to quantify differences between animal groups.

For variables that have multiple variates per animal (such as $Entropy_{MEAN}$ calculated from multiple channels, Fig. 6C-D), mixed effects models are constructed in the MATLAB Statistics and Machine Learning Toolbox (***Pinheiro and Bates, 1996***; ***MATLAB, 2021***). $Entropy_{MEAN}$ and similarly $Entropy_{STD}$ (not shown) and $Entropy_{MEAN,EVENT}$ and similarly $Entropy_{STD,EVENT}$ (not shown) are modelled via mixed effects as

$$Entropy_{MEAN} = Animal\ Type + (1|channel) + (1|animal\ ID) \tag{5}$$

$$\begin{aligned} Entropy_{MEAN,EVENT} &= Event\ Type + Animal\ Type + \\ CoactivityType &+ (1|channel) + (1|animal\ ID) + (1|Entropy_{MEAN}) \end{aligned} \tag{6}$$

where $1|$ indicates random effects.

In Eq. (6), and depicted in Fig. 6C-D, the computed metric $Entropy_{MEAN}$ is the outcome variable; the animal type $(control/HF)$ a fixed effect; and the channel number $(1-16)$ and the $animal\ ID$ random effects. The analysis of $Entropy_{STD}$ follows by replacing 'MEAN' with 'STD'.

In Eq. (6) the model $Entropy_{MEAN,EVENT}$ is shown and refers to entropy mean data within event regions where the model for mean entropy data outside event regions is $Entropy_{MEAN,NON-EVENT}$. In this way, models are constructed for event / non-event, mean / std entropy as the outcome variable; the event type (event / non-event), the animal type (control / HF), and coactivity computation type (mean / std) are fixed effects; and channel number, animal ID, and entropy (type matching the outcome entropy's type, mean or std) are random effects.

For all analyses using mixed effects modeling, the β coefficients (fixed effects estimates), p-values, effect sizes (d_{RM} based on repeated measures Cohen's d_{RM}, (***Lakens, 2013***)), 95% confidence intervals (CI) of β coefficients (lower, upper bounds) are reported in results in (β, $\pm CI$, d_{RM}, p) format. The β coefficients indicate the adjusted differences (units matching the outcome variable's unit) in one group compared to the other. For analyses with independent samples, p-values and independent samples effect sizes (d, based on Cohen's d) are reported in (p, d) format. For all analyses, a two-sided $p < 0.05$ denoted statistical significance.

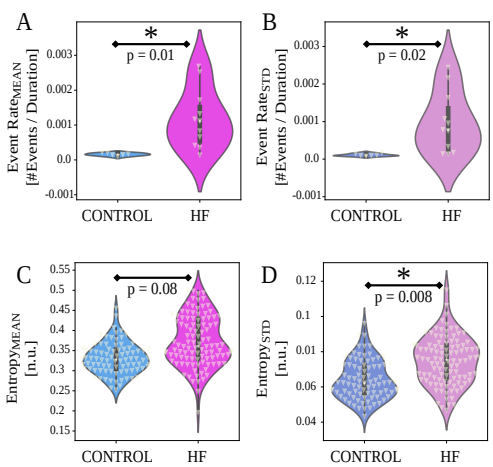

Figure 6. Event rate (ER) and entropy results between control and HF animals (horizontal axes). White triangles indicate data points. A-B) Heart failure (HF) group animals show significantly higher ER_{MEAN} and ER_{STD} compared to control group $(p < 0.05)$. C-D) HF group animals show significantly higher entropy variability ($Entropy_{STD}$, Eq. (6), $p = 0.008$, in D), however no significant difference in $Entropy_{MEAN}$ (Eq. (6), $p = 0.08$, in C). For ER, p-values are calculated from two-sample t-test or Wilcoxon rank-sum tests, depending on normality. For entropy, p-values are calculated from linear mixed effects (LME, Eq. (6)) detailed in Methods.

Results

Neural activity was measured over 16 channels along with simultaneous left ventricular pressure (LVP) for approximately six hours of continuous recordings per animal. Representative neural activity recording for a single channel, LVP, and representative spike trains are displayed for control and heart failure animals in Fig. 1A. A total of 17 Yorkshires (6 control, 11 HF, Fig. 1D) underwent the terminal experiment described in Fig. 1E. Upon the signal processing pipeline described above, we computed two event rate

measures per animal as the final product representing the cofluctuations (ER_{MEAN}, ER_{STD}). As the metric representing the neural specificity, we computed two entropy measures per channel ($Entropy_{MEAN}$, $Entropy_{STD}$), resulting in a total of sixteen $Entropy_{MEAN}$ and sixteen $Entropy_{STD}$ per animal. Finally, we used these metrics to quantify: i) neural population dynamics (i.e., ER_{MEAN}, ER_{STD}), ii) neural specificity to target LVP, or cardiac control (i.e., $Entropy_{MEAN}$, $Entropy_{STD}$), and iii) Linkage between neural population dynamics and specificity (i.e., $Entropy_{MEAN,EVENT}$, $Entropy_{STD,EVENT}$).

Stellate Ganglion in Heart Failure Exhibits High Event Rate

Fig. 6A-B show event rate outcomes grouped by heart failure (HF) models and controls. HF animals show significantly higher event rates compared to control animals for both ER_{MEAN} ($p = 0.011$, effect size $d = 1.59$) and ER_{STD} ($p = 0.023$, $d = 1.48$). The cofluctuation time series for each animal is depicted in Fig. 8, where the event time series are computed. The 'events' or short-lived intervals where high cofluctuations exist are shown as level 1, leading to the event time series in Fig. 9. We observe that the cofluctuations are more localized in HF animals with greater heterogeneity.

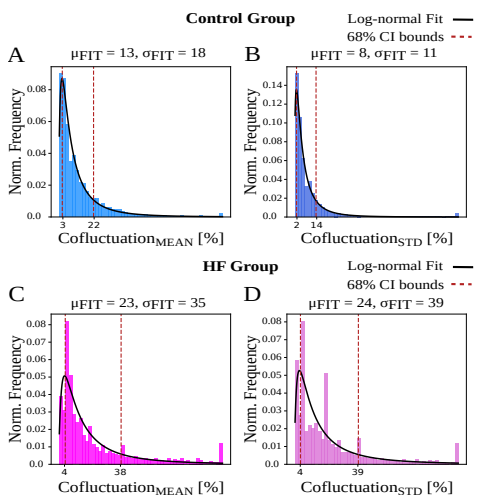

Figure 7. Cofluctuation histograms (calculated from mean or standard deviation of sliding spike rate, referred as $Cofluctuation_{MEAN}$ and $Cofluctuation_{STD}$, respectively) and log-normal fits for each animal group. μ_{FIT} and σ_{FIT} are the respective mean and standard deviation (STD) of fitted distribution, used for 68% confidence interval bounds. A-B) Control animals have narrower bounds and represent a better fit to log-normal distribution. C-D) Heart failure (HF) animals display more heavily skewed distributions that indicate heavy tails.

HF Animal Models Have Heavy Tailed Cofluctuation Distributions

We qualitatively explored the statistical distribution of the cofluctuation time series. Fig. 7 shows log-normal fits for each animal group for $Cofluctuation_{MEAN}$ and $Cofluctuation_{STD}$ time series, along with 68% confidence interval (CI) bounds, mean of fit (μ_{FIT}) and standard deviation of fit (σ_{FIT}). Control animals (Fig. 7A-B) exhibit narrow confidence intervals, lower (μ_{FIT}) and (σ_{FIT}) values, and tighter log-normal fits. In contrast, HF animals (Fig. 7C-D) exhibit wider confidence intervals, higher (μ_{FIT}) and (σ_{FIT}) values, and poorer log-normal fits. Of note, HF animals have heavy tails ranging further outside of confidence bounds.

Stellate Ganglion Shows Greater Variation in Neural Specificity to LVP in Heart Failure

We next examined the neural specificity to LVP, quantified by entropy measures in Eq. (6). Fig. 6C-D shows $Entropy_{MEAN}$ and $Entropy_{STD}$, grouped by animals. Compared to the control group, stellate ganglion of HF animals exhibited significantly higher $Entropy_{STD}$ (variation in entropy, Fig. 6D, adjusted $\beta = 0.01$ n.u., 95% $CI = \pm 0.01$ n.u., $d_{RM} = 0.73$, $p = 0.009$). However, there is no significant difference in $Entropy_{MEAN}$ (mean entropy) between animal groups. (Fig. 6C, $\beta = 0.04$ n.u., ± 0.05 n.u., $d_{RM} = 0.82$, $p = 0.087$).

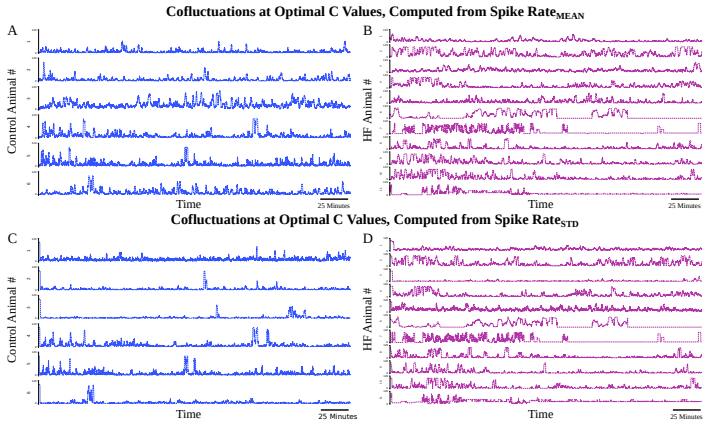

Figure 8. Cofluctuations time series at convergent C values for each animal. A) Cofluctuations from coactivity calculation from mean of sliding spike rate for control animals. B) Cofluctuations from coactivity calculation from mean of sliding spike rate for HF animals. C) Cofluctuations from coactivity calculation from standard deviation of sliding spike rate for control animals. D) Cofluctuations from coactivity calculation from standard deviation of sliding spike rate for HF animals.

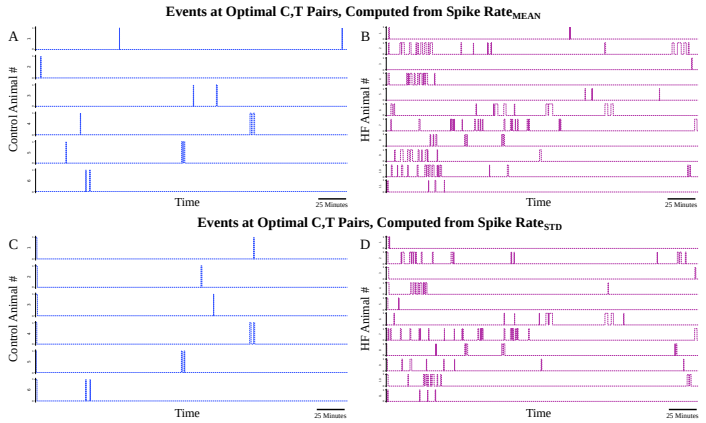

Figure 9. Events time series at convergent (C, T) pairs for each animal. A) Events from coactivity calculation from mean of sliding spike rate for control animals. B) Events from coactivity calculation from mean of sliding spike rate for HF animals. C) Events from coactivity calculation from standard deviation of sliding spike rate for control animals. D) Events from coactivity calculation from standard deviation of sliding spike rate for HF animals.

Neural Network Activity and Cardiac Control Linkage Depends on Animal Group and Cofluctuation Magnitude

We explored the nature of cardiac control inside and outside short duration regions of high cofluctuation, i.e. 'events', characterized by strongly coherent stellate neural activity patterns. Insight into how these events may be relevant to cardiac control is considered here in the context of how control differs inside and outside events and termed 'event entropy'.

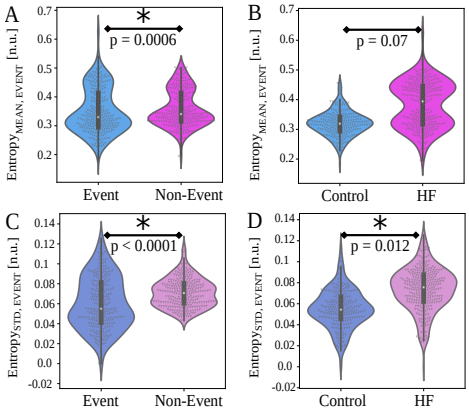

Figure 10. Event entropy Eq. (6) investigation involved consideration of entropy values inside and outside of event regions. A) There is significant difference between in $Entropy_{MEAN,EVENT}$ and $Entropy_{STD,EVENT}$ across all animals ($p = 0.0006$). B) There is no significant difference in $Entropy_{MEAN,EVENT}$ between animal groups ($p = 0.07$). C) There is significant difference in $Entropy_{STD,EVENT}$ between events and non-events across all animals ($p < 0.0001$). D) There is significant difference in $Entropy_{STD,EVENT}$ between animal groups ($p < 0.012$).

First, we studied the extent to which event entropy differs inside and outside of events (Fig. 10A, C, event type as fixed effect in Eq. (9)). Second, we studied whether event entropy is sensitive to the animal type characterized here as control or HF (Fig. 10B, D, animal type as fixed effect in Eq. (9)).

Regardless of the animal group, $Entropy_{MEAN,NON-EVENT}$ significantly exceeds $Entropy_{MEAN,EVENT}$ (Fig. 10A, $\beta = 0.007$ n.u., ± 0.004 n.u., $d_{RM} = 0.07$, $p < 0.001$). Similarly, $Entropy_{STD,NON-EVENT}$ significantly exceeds $Entropy_{STD,EVENT}$ (Fig. 10C, $\beta = 0.01$ n.u., ± 0.002 n.u., $d_{RM} = 0.29$, $p < 0.001$). An examination of the contribution of each animal group showed no significant difference between groups for $Entropy_{MEAN,EVENT}$ (Fig. 10B, $\beta = 0.06$ n.u., ± 0.05 n.u., $d_{RM} = 1.13$, $p = 0.07$). On the other hand, HF animals exhibited an increase in $Entropy_{STD,EVENT}$ compared to control animals (Fig. 10D, $\beta = 0.02$ n.u., ± 0.02 n.u., $d_{RM} = 0.75$, $p = 0.012$). These analyses imply that the linkage between neural network function and cardiac control differs inside and outside of cofluctuation events and between animal groups in the stellate ganglion.

Discussion

In this work, we performed a novel investigation of SG neural population dynamics and neural specificity to continuous left ventricular pressure in control and heart failure Yorkshire pigs. The methods in this work are intended to measure the way population neural activity relates to closed-loop control of a target and how that computation changes in diseased states. This was applied here to closed-loop control of cardiac output where the assumed target was LVP.

The methods in this work involved

- *Neural Specificity* A measure of bias in neural activity toward 'sampling' of specific target states. The target specificity is a contrastive measure that compares neural sampling of a target relative to random sampling of the same target.
- *Neural Specificity Coherence* Entropy of neural specificity was used to measure coherence of neural specificity as a function of time.
- *Cofluctuation Events* The degree of coactivity in the dynamics of the mean and its standard deviation was measured between pairs of channels from minimum to maximum physical separation and this exposed short duration 'events' when cofluctuation was unusually high.

- *Event Entropy* Functional significance of cofluctuation events was evaluated by comparing differences in the degree of neural specificity coherence inside and outside of events.

Prevalence of Short-Lived Cofluctuations in SG Activity in HF

In prior work, we identified neural specificity toward near-peak systole of the LVP waveform in control animals (***Sudarshan et al., 2021***). Application of this metric and the construction of a related coherence measure provided insight into differences in neural processing dynamics between control and HF animals. Our results show that cardiac control exerted within diseased states has greater variation in entropy and thus less consistency for heart failure animals compared to control animals. This finding may extend to other pathologies for which the cardiac control hierarchy is disrupted.

Neural Network Activity is Linked to Cardiac Control

Based on the effect size (d_{RM}), event entropy magnitude appears to be higher with greater variation observed in HF animals compared to control animals (Fig. 10B-D). This implies a level of increased unpredictability and increased difficulty in cardiac control for animals in heart failure over control animals.

A limitation of this result is that the effect sizes for event versus non-event comparisons are small to medium, which potentially indicates a larger study is necessary to better understand the physiological contributions from event type. Another limitation of the study lies in the absence of multiple-class pathologies (i.e., different heart failure models or other reproducible models) and in the absence of stratified pathologies (i.e., animal models with varying degrees of heart failure). Measurement of these neurocardiac metrics during slow, quasi-static application of clinically-relevant stressors (***Akeju and Brown, 2017***; ***Chamadia et al., 2019***) should provide unique opportunities to investigate unresolved questions. Future studies should focus on expanding the dataset to examine how these metrics change with varying pathologies or varying disease models.

Conclusion

Our findings are aligned with a growing consensus in neuroscience that changes in neural activity through space and time are associated with the onset and development of specific pathologies. Neuroscience studies in different domains have been undertaken to understand the underpinnings of pathologies and information processing. For instance, spatiotemporal brain-wide fluctuations are reported to reveal major depression vulnerability (***Hultman et al., 2018***). Another study reported that brain's functional connectivity is driven by high-amplitude cofluctuations and that these cofluctuations encode subject-specific information during experimental tasks (***Esfahlani et al., 2020***). Furthermore, the neural specificity phenomenon was observed within the context of visual neural circuits with the difference being that neural activity aperiodically locks to specific visual stimuli (***Miller et al., 2014***). In our work, the primary observation has been that event-based processing within the stellate ganglion and its relationship to cardiac control is strongly sensitive to disruptions of the cardiac milieu. Understanding the evolution of networked stellate ganglion processing inside and outside these high cofluctuation time domains will provide insight into the nature of how cardiac control is variously exerted in the presence and absence of pathology.

Acknowledgments

This work was funded by the National Institutes of Health, Office of The Director DP2 OD024323-01 and NHLBI R01 HL159001. NZG was funded by the National Science Foundation American Society of Engineering Education's Engineering Fellows Postdoctoral Fellowship Award ID #2127509. The authors would like to thank Prof. Jeffrey Ardell for fruitful discussions.

References

Ajijola OA, Chatterjee NA, Gonzales MJ, Gornbein J, Liu K, Li D, Paterson DJ, Shivkumar K, Singh JP, Herring N. Coronary sinus neuropeptide Y levels and adverse outcomes in patients with stable chronic heart failure. JAMA cardiology. 2020; 5(3):318–325.

Ajijola OA, Lellouche N, Bourke T, Tung R, Ahn S, Mahajan A, Shivkumar K. Bilateral cardiac sympathetic denervation for the management of electrical storm. Journal of the American College of Cardiology. 2012; 59(1):91–92.

Ajijola OA, Wisco JJ, Lambert HW, Mahajan A, Stark E, Fishbein MC, Shivkumar K. Extracardiac neural remodeling in humans with cardiomyopathy. Circulation: Arrhythmia and Electrophysiology. 2012; 5(5):1010–1116.

Ajijola OA, Yagishita D, Patel KJ, Vaseghi M, Zhou W, Yamakawa K, So E, Lux RL, Mahajan A, Shivkumar K. Focal myocardial infarction induces global remodeling of cardiac sympathetic innervation: neural remodeling in a spatial context. American Journal of Physiology-Heart and Circulatory Physiology. 2013; 305(7):H1031–H1040.

Ajijola OA, Yagishita D, Reddy NK, Yamakawa K, Vaseghi M, Downs AM, Hoover DB, Ardell JL, Shivkumar K. Remodeling of stellate ganglion neurons after spatially targeted myocardial infarction: neuropeptide and morphologic changes. Heart Rhythm. 2015; 12(5):1027–1035.

Akeju O, Brown EN. Neural oscillations demonstrate that general anesthesia and sedative states are neurophysiologically distinct from sleep. Current opinion in neurobiology. 2017; 44:178–185.

Ardell J, Andresen M, Armour J, Billman G, Chen PS, Foreman R, Herring N, O'leary D, Sabbah HN, Schultz HD, et al. Translational neurocardiology: preclinical models and cardioneural integrative aspects. The Journal of physiology. 2016; 594(14):3877–3909.

Armour J. Synaptic transmission in the chronically decentralized middle cervical and stellate ganglia of the dog. Canadian journal of physiology and pharmacology. 1983; 61(10):1149–1155.

Armour J. Activity of in situ stellate ganglion neurons of dogs recorded extracellularly. Canadian journal of physiology and pharmacology. 1986; 64(2):101–111.

Armour J, Collier K, Kember G, Ardell J. Differential selectivity of cardiac neurons in separate intrathoracic autonomic ganglia. American Journal of Physiology-Regulatory, Integrative and Comparative Physiology. 1998; 274(4):R939–R949.

Blaye-Felice MS, Hamon D, Sacher F, Pascale P, Rollin A, Duparc A, Mondoly P, Derval N, Denis A, Cardin C, et al. Premature ventricular contraction-induced cardiomyopathy: related clinical and electrophysiologic parameters. Heart Rhythm. 2016; 13(1):103–110.

Chamadia S, Pedemonte JC, Hahm EY, Mekonnen J, Ibala R, Gitlin J, Ethridge BR, Qu J, Vazquez R, Rhee J, et al. Delta oscillations phase limit neural activity during sevoflurane anesthesia. Communications biology. 2019; 2(1):1–10.

Chen WW, Xiong XQ, Chen Q, Li YH, Kang YM, Zhu GQ. Cardiac sympathetic afferent reflex and its implications for sympathetic activation in chronic heart failure and hypertension. Acta Physiologica. 2015; 213(4):778–794.

Deyell MW, Krahn AD, Goldberger JJ. Sudden cardiac death risk stratification. Circulation research. 2015; 116(12):1907–1918.

Esfahlani FZ, Jo Y, Faskowitz J, Byrge L, Kennedy DP, Sporns O, Betzel RF. High-amplitude cofluctuations in cortical activity drive functional connectivity. Proceedings of the National Academy of Sciences. 2020; 117(45):28393–28401.

Gao L, Pan YX, Wang WZ, Li YL, Schultz HD, Zucker IH, Wang W. Cardiac sympathetic afferent stimulation augments the arterial chemoreceptor reflex in anesthetized rats. Journal of Applied Physiology. 2007; 102(1):37–43.

Gao L, Schultz HD, Patel KP, Zucker IH, Wang W. Augmented input from cardiac sympathetic afferents inhibits baroreflex in rats with heart failure. Hypertension. 2005; 45(6):1173–1181.

Han S, Kobayashi K, Joung B, Piccirillo G, Maruyama M, Vinters HV, March K, Lin SF, Shen C, Fishbein MC, et al. Electroanatomic remodeling of the left stellate ganglion after myocardial infarction. Journal of the American College of Cardiology. 2012; 59(10):954–961.

Hori Y, Temma T, Wooten C, Sobowale C, Chan C, Swid M, Ajijola OA. Cardiac afferent signaling partially underlies premature ventricular contraction–induced cardiomyopathy. Heart Rhythm. 2021; 18(9):1586–1595.

Hultman R, Ulrich K, Sachs BD, Blount C, Carlson DE, Ndubuizu N, Bagot RC, Parise EM, Vu MAT, Gallagher NM, et al. Brain-wide electrical spatiotemporal dynamics encode depression vulnerability. Cell. 2018; 173(1):166–180.

Kember G, Armour JA, Zamir M. Neural control hierarchy of the heart has not evolved to deal with myocardial ischemia. Physiological genomics. 2013; 45(15):638–644.

Lakens D. Calculating and reporting effect sizes to facilitate cumulative science: a practical primer for t-tests and ANOVAs. Frontiers in psychology. 2013; p. 863.

Ma R, Zucker IH, Wang W. Central gain of the cardiac sympathetic afferent reflex in dogs with heart failure. American Journal of Physiology-Heart and Circulatory Physiology. 1997; 273(6):H2664–H2671.

MATLAB. version 7.10.0 (R2010a). Natick, Massachusetts: The MathWorks Inc.; 2021.

Mehra R, Tjurmina OA, Ajijola OA, Arora R, Bolser DC, Chapleau MW, Chen PS, Clancy CE, Delisle BP, Gold MR, et al. Research Opportunities in Autonomic Neural Mechanisms of Cardiopulmonary Regulation: A Report From the National Heart, Lung, and Blood Institute and the National Institutes of Health Office of the Director Workshop. JACC: Basic to Translational Science. 2022; .

Miller JeK, Ayzenshtat I, Carrillo-Reid L, Yuste R. Visual stimuli recruit intrinsically generated cortical ensembles. Proceedings of the National Academy of Sciences. 2014; 111(38):E4053–E4061.

Nakamura K, Ajijola OA, Aliotta E, Armour JA, Ardell JL, Shivkumar K. Pathological effects of chronic myocardial infarction on peripheral neurons mediating cardiac neurotransmission. Autonomic Neuroscience. 2016; 197:34–40.

Pinheiro JC, Bates DM. Unconstrained parametrizations for variance-covariance matrices. Statistics and computing. 1996; 6(3):289–296.

Sudarshan KB, Hori Y, Swid MA, Karavos AC, Wooten C, Armour JA, Kember G, Ajijola OA. A novel metric linking stellate ganglion neuronal population dynamics to cardiopulmonary physiology. American Journal of Physiology-Heart and Circulatory Physiology. 2021; 321(2):H369–H381.

Vaseghi M, Barwad P, Malavassi Corrales FJ, Tandri H, Mathuria N, Shah R, Sorg JM, Gima J, Mandal K, Sàenz Morales LC, et al. Cardiac sympathetic denervation for refractory ventricular arrhythmias. Journal of the American College of Cardiology. 2017; 69(25):3070–3080.

Vaseghi M, Zhou W, Shi J, Ajijola OA, Hadaya J, Shivkumar K, Mahajan A. Sympathetic innervation of the anterior left ventricular wall by the right and left stellate ganglia. Heart rhythm. 2012; 9(8):1303–1309.

Virtanen P, Gommers R, Oliphant TE, Haberland M, Reddy T, Cournapeau D, Burovski E, Peterson P, Weckesser W, Bright J, et al. SciPy 1.0: fundamental algorithms for scientific computing in Python. Nature methods. 2020; 17(3):261–272.

Wang HJ, Rozanski GJ, Zucker IH. Cardiac sympathetic afferent reflex control of cardiac function in normal and chronic heart failure states. The Journal of physiology. 2017; 595(8):2519–2534.

Wang HJ, Wang W, Cornish KG, Rozanski GJ, Zucker IH. Cardiac sympathetic afferent denervation attenuates cardiac remodeling and improves cardiovascular dysfunction in rats with heart failure. Hypertension. 2014; 64(4):745–755.

Wang W, Zucker IH. Cardiac sympathetic afferent reflex in dogs with congestive heart failure. American Journal of Physiology-Regulatory, Integrative and Comparative Physiology. 1996; 271(3):R751–R756.

Wang WZ, Gao L, Wang HJ, Zucker IH, Wang W. Interaction between cardiac sympathetic afferent reflex and chemoreflex is mediated by the NTS AT1 receptors in heart failure. American Journal of Physiology-Heart and Circulatory Physiology. 2008; 295(3):H1216–H1226.

Yoshie K, Rajendran PS, Massoud L, Kwon O, Tadimeti V, Salavatian S, Ardell JL, Shivkumar K, Ajijola OA. Cardiac vanilloid receptor-1 afferent depletion enhances stellate ganglion neuronal activity and efferent sympathetic response to cardiac stress. American Journal of Physiology-Heart and Circulatory Physiology. 2018; 314(5):H954–H966.

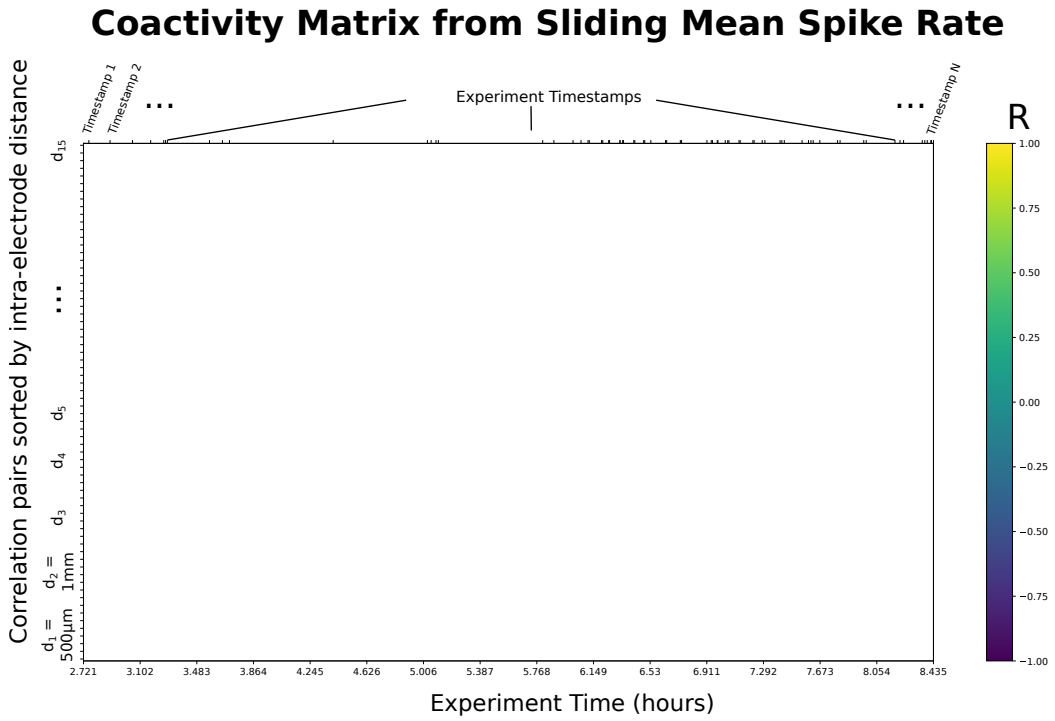

Figure 11. Supplementary Figure for Fig. 4A. A sample coactivity matrix computed from the sliding (rolling) mean of spike rate for the 16-channel linear mapping array (LMA) used throughout an experiment. Y axis shows correlation pairs (i.e., Channel 1 vs. Channel 2). Correlation pairs are stacked such that the lowest row corresponds to channels separated by the minimum inter-electrode distance ($d_1 = 500\mu m$, 1-electrode away), and inter-electrode distance increasing from a separation of 1 to 15 channels at the top. For instance, the highest row shows the pair separated by the maximum inter-electrode distance ($d_{15} = 15 * 500\mu m = 7.5mm$, 15-electrodes away). The order corresponds to the super-diagonals of the 16 x 16 correlation matrix. Y axis includes 120 comparisons for 16 channels, colors indicate Pearson's correlation coefficients specified in the color legend.

645 **Yoshie K**, Rajendran PS, Massoud L, Mistry J, Swid MA, Wu X, Sallam T, Zhang R, Goldhaber JI, Salavatian S,
646 et al. Cardiac TRPV1 afferent signaling promotes arrhythmogenic ventricular remodeling after myocardial
647 infarction. JCI insight. 2020; 5(3).